QUARTERLY JOURNAL OF THE ROYAL METEOROLOGICAL SOCIETY
Q. J. R. Meteorol. Soc. **134**: 1269–1285 (2008)
Published online 9 July 2008 in Wiley InterScience
(www.interscience.wiley.com) DOI: 10.1002/qj.271

Axisymmetric, nearly inviscid circulations in non-condensing radiative-convective atmospheres

Rodrigo Caballero,[a]* Raymond T. Pierrehumbert[b] and Jonathan L. Mitchell[c]
[a] *Meteorology and Climate Centre, School of Mathematical Sciences, University College Dublin, Ireland*
[b] *Department of the Geophysical Sciences, University of Chicago, Illinois, USA*
[c] *Department of Astronomy and Astrophysics, University of Chicago, Illinois, USA*

ABSTRACT: We study the steady-state axisymmetric circulation of nearly inviscid, compressible atmospheres with no condensible component. Assuming simplified non-grey radiative transfer and instantaneous adjustment to convective neutrality, we present an analytical theory for the depth, width and strength of the Hadley cell in terms of the planetary radius and rotation rate, insolation, optical depth and atmospheric composition. Under equatorially symmetric insolation, the Hadley cell width predicted by the present theory is generally very close to the Boussinesq, Newtonian cooling result of Held and Hou. We also introduce a new scaling theory for Hadley cell width under solstitial insolation conditions. The theory compares favourably with axisymmetric numerical results and also with full general-circulation model simulations of Mars and Snowball Earth.

KEY WORDS Hadley cell; radiative-convective equilibrium; Mars; Snowball Earth

Received 25 July 2007; Revised 4 April 2008; Accepted 12 May 2008

1. Introduction

Despite a venerable history dating back at least to Hadley (1735), a complete theory for the zonal-mean atmospheric circulation has yet to emerge. Ideally, such a theory would quantitatively predict the structure and intensity of the circulation given only planetary parameters such as radius, rotation rate, gravity, obliquity, solar constant and details of the atmospheric composition and opacity. It would apply not only to Earth's modern climate, but to ancient paleoclimates and planetary atmospheres as well, providing an important constraint on the detailed predictions provided by general circulation models (GCMs).

An important step towards such a theory was taken by Schneider (1977) and Held and Hou (1980, henceforth HH), who noted that the twin requirements of geostrophic (or cyclostrophic) balance and angular momentum (AM) conservation in a nearly-inviscid atmosphere impose a very strong constraint on the horizontal temperature structure; the further requirement of energy conservation then leads to an elegantly simple prediction for the width of the tropical meridional overturning or Hadley cell. Making the small-angle approximation, HH obtain the expression

$$\varphi_{\mathrm{H}} = \left(\frac{5}{3} \frac{g H_{\mathrm{t}} \Delta_{\mathrm{H}}}{\Omega^2 a^2} \right)^{1/2}, \qquad (1)$$

where φ_{H} is the latitude of the cell's poleward edge, g is the gravitational acceleration, H_{t} is the height of the cell, Δ_{H} is the fractional Equator–Pole drop in radiative-convective equilibrium temperature, a is the planetary radius and Ω the rotation rate.

Equation (1) was derived under the Boussinesq and Newtonian cooling approximations. In the closing section of their paper, HH discuss how these assumptions might be relaxed to accommodate compressible, radiative-convective atmospheres. Our first purpose here is to take up this lead, using a specific radiative-convective model to derive a formula analogous to (1) but adapted to the radiative-convective setting.

We limit our attention to atmospheres which are effectively dry, i.e. where condensation plays a negligible role. As discussed below, such atmospheres are of interest in the planetary and paleoclimatological context. Dryness also simplifies the treatment by avoiding the need to deal with transport and release of latent heat and the complexities of moist convection. Moreover, in a non-condensing atmosphere all gases may be considered well-mixed, which avoids the difficult non-linearities arising when the distribution of absorbers, and thus the radiative driving, depends on the circulation itself.

Dry atmospheres have some unusual features when compared to Earth's. One is extreme seasonality. Earth's large oceanic thermal inertia helps keep maximum surface temperatures within the Tropics in all seasons, but on dry planets we expect a solid surface with low thermal inertia, which can lead to a heating maximum at or near the Pole during solstice. A second aim of this paper is to study the dry axisymmetric circulation under this extreme solstitial heating gradient. Furthermore, in a

* Correspondence to: Rodrigo Caballero, Meteorology and Climate Centre, School of Mathematical Sciences, University College Dublin, Belfield, Dublin 4, Ireland. E-mail: rodrigo.caballero@ucd.ie

dry atmosphere both rising and subsiding branches of the tropospheric Hadley cell should follow the dry adiabat, raising some interesting questions about the energetics of the circulation (see Pierrehumbert, 2005, and Section 6 below); the third aim of the paper is to shed some light on these questions.

We retain throughout the axisymmetric and nearly inviscid assumptions of HH. Our results are therefore incomplete as a description of the general circulation, since large-scale zonally asymmetric eddies can be expected to play a leading role in the maintenance of the mean flow (Walker and Schneider, 2006). Nonetheless, a more detailed understanding of the axisymmetric flow seems a useful step on the way to a comprehensive theory for the general circulation. As noted by HH, the importance of mixing by large-scale eddies may best be appreciated by studying the circulation which develops in their absence.

Dry Hadley cells occur in a number of planetary and deep-time paleoclimate problems. In the cold climate of a fully glaciated Snowball Earth there is so little water vapour in the atmosphere that the Hadley cell dynamics are effectively dry; the Hadley cell heat transports can significantly affect deglaciation, yet the behaviour of the circulation as revealed in GCMs raises a number of challenging questions that call for more fundamental study (Pierrehumbert, 2005).

The Hadley cell in the present Martian climate is also unaffected by latent heat release; this cell is a major player in the general circulation of Mars, and tends to be more global in extent than Earth's Hadley cell (Lewis, 2003). One cannot appeal to a lower rotation rate on Mars to account for the more global circulation, since Mars has a similar rotation rate to Earth. The global extent must be due to some combination of the small size of the planet, the radiative driving parameters, and the low thermal inertia of the planet's surface. While all these effects have been qualitatively discussed previously, putting them in the context of a general Hadley cell theory can do much to sharpen thinking about the effect of the various parameters. In particular, it will provide a better basis for understanding the nature of the Hadley circulation on a hypothetical Early Mars warmed by the effects of a dense CO_2 atmosphere with surface pressure perhaps as large as 2 bars (Forget and Pierrehumbert, 1997).

The global Hadley circulation of Titan may be strongly influenced by condensation of methane, but current thinking about the planet embraces a range of possible degrees of dryness, depending on the distribution of methane sources at the surface (Mitchell *et al*., 2006). Therefore, the dry limit is of interest on Titan as well, as an end-member of the family of possible circulations.

The paper proceeds as follows. We begin in section 2 by setting out our model equations and assumptions. An important aspect is the choice of radiative scheme. The grey gas scheme is often used in theoretical work, but is a poor approximation to the real absorption spectrum of most atmospheres. As shown by Weaver and Ramanathan (1995) (henceforth WR), inclusion of non-grey effects makes a qualitative difference, giving radiative equilibrium solutions with a smaller surface temperature discontinuity and a generally greater lapse rate. These differences will inevitably affect convection and thus tropopause height, which is a key concern here. By the same token, it is important to consider the effects of pressure broadening, which also has an important effect on the stability of radiative equilibrium states. We adopt WR's scheme, which is both analytically tractable and more realistic than the grey-gas approximation, and we also include a simplified treatment of pressure broadening effects.

Section 3 presents an analytical derivation of tropopause level and the radiative-convective equilibrium temperature structure. A key result here is that tropopause level is independent of latitude, a feature related to the meridionally constant optical depth in an atmosphere with well-mixed radiative absorbers. This allows us in section 4 to follow HH's procedure to derive the width of the Hadley cell. Section 5 shows that the width thus derived actually differs from HH's, but only by a factor which is generally close to 1 over a broad parameter range. Section 6 again follows HH by using the cell width derived previously to compute the energy transport and mass flux carried by the circulation. Section 7 presents a theory for Hadley cell extent under solstitial conditions. Section 8 compares the present theory with full GCM simulations of Snowball Earth and modern Mars, both of which have essentially dry atmospheres. Finally, section 9 summarises our conclusions.

2. Model description and numerical solutions

2.1. Dynamics

We consider the axisymmetric primitive equations using pressure as vertical coordinate:

$$\frac{\partial u}{\partial t} = -\frac{v}{a}\frac{\partial u}{\partial \varphi} - \omega\frac{\partial u}{\partial \eta} + \frac{uv}{a}\tan\varphi + 2\Omega v\sin\varphi + \frac{\partial}{\partial \eta}\left(\frac{\eta^2}{H^2}\nu\frac{\partial u}{\partial \eta}\right), \tag{2}$$

$$\frac{\partial v}{\partial t} = -\frac{v}{a}\frac{\partial v}{\partial \varphi} - \omega\frac{\partial v}{\partial \eta} - \frac{u^2}{a}\tan\varphi - 2\Omega u\sin\varphi - \frac{1}{a}\frac{\partial \Phi}{\partial \varphi} + \frac{\partial}{\partial \eta}\left(\frac{\eta^2}{H^2}\nu\frac{\partial v}{\partial \eta}\right), \tag{3}$$

$$\frac{\partial \ln\Theta}{\partial t} = -\frac{v}{a}\frac{\partial \ln\Theta}{\partial \varphi} - \omega\frac{\partial \ln\Theta}{\partial \eta} + \frac{Q_\mathrm{r}}{T} + \frac{Q_\mathrm{c}}{T} + \frac{1}{\Theta}\frac{\partial}{\partial \eta}\left(\frac{\eta^2}{H^2}\mu\frac{\partial \Theta}{\partial \eta}\right), \tag{4}$$

$$\frac{\partial \omega}{\partial \eta} = -\frac{1}{a\cos\varphi}\frac{\partial}{\partial \varphi}(v\cos\varphi), \tag{5}$$

DOI: 10.1002/qj

$$\frac{\partial \Phi}{\partial \eta} = -\frac{RT}{\eta}, \tag{6}$$

$$\text{where } \eta = \frac{p}{p_s} \tag{7}$$

is pressure adimensionalised by surface pressure and φ is latitude; u, v and ω are respectively the zonal, meridional and vertical (pressure) velocity, T is temperature, Θ is potential temperature, Φ is the geopotential, and a and Ω are the planetary radius and rotation rate. Vertical diffusion of momentum and potential temperature is included with spatially uniform kinematic diffusivities ν and μ respectively. $H = RT/g$ is the local pressure scale height, with R the gas constant for the atmosphere in question and g the surface gravitational acceleration. Q_r is the radiative heating rate (see below). Q_c is the convective heating rate, assumed strong enough to maintain neutral stability in the troposphere at all times. In practice, the numerical simulations presented here employ standard 'hard' dry adiabatic adjustment: at each time step, any statically unstable layers are instantaneously rearranged to be statically neutral while conserving dry static energy.

2.2. Radiation

We use the two-stream plane-parallel approximation to radiative transfer,

$$\frac{\mathrm{d}I_\lambda^+}{\mathrm{d}\tau_\lambda} = -I_\lambda^+ + \pi B_\lambda, \tag{8}$$

$$\frac{\mathrm{d}I_\lambda^-}{\mathrm{d}\tau_\lambda} = I_\lambda^- - \pi B_\lambda, \tag{9}$$

where λ subscripts indicate wavelength dependence, I_λ^+ and I_λ^- are respectively upward and downward monochromatic irradiances, B_λ is the Planck function and τ_λ is the optical path measured from the surface,

$$\tau_\lambda = D\frac{p_s}{g}\int_\eta^1 k_\lambda\, q\, \mathrm{d}\eta, \tag{10}$$

with k_λ the mass absorption coefficient, q the absorber mixing ratio, and $D \approx 1.66$ is the 'diffusivity factor' approximately accounting for integration of radiance over a hemisphere (Elsasser, 1942).

For wavelength dependence, we follow WR and assume an atmosphere transparent to solar radiation but with a piecewise-constant long-wave absorption profile. WR focused on the case of water vapour, using an absorption profile which was constant and positive throughout the spectrum except for a transparent band representing the water vapour window, where the absorption coefficient was set to zero. Here, we are more interested in gases such as CO_2, which has the opposite profile: it is zero everywhere outside a few narrow bands. To capture the basic character of this absorption spectrum, we use a 'top hat' profile:

$$k_\lambda = \begin{cases} k_b & \text{for } \lambda_1 < \lambda < \lambda_2, \\ 0 & \text{otherwise,} \end{cases} \tag{11}$$

where k_b is a constant. We refer to the resulting radiative model as 'band-semigrey'.

A broadband, Planck-weighted optical depth can be defined as

$$\tau = \beta\, \tau_b$$

where τ_b is the in-band optical depth given by (10) with k_b replacing k_λ, and

$$\beta = \int_{\lambda_1}^{\lambda_2} \frac{\pi B_\lambda}{\sigma T^4}\, \mathrm{d}\lambda$$

is an equivalent bandwidth. The classical grey-gas approximation is recovered by setting $\beta = 1$. Figure 1 shows β for a 2 μm interval centred at 15 μm, a reasonable choice to mimic absorption by CO_2. Though β is clearly a function of temperature, we follow WR in neglecting this dependence.

With these assumptions, (8)–(9) can be integrated spectrally and solved for the broadband upward flux $I^+ \equiv \int_0^\infty I_\lambda^+\, \mathrm{d}\lambda$, yielding

$$I^+(\tau) = \sigma T_s^4\, \mathrm{e}^{-\tau/\beta} + \int_0^{\tau/\beta} \sigma T^4\, \mathrm{e}^{(\tau'-\tau)/\beta}\, \mathrm{d}\tau', \tag{12}$$

with an analogous solution for the downward flux. The surface has been assumed to be a black body with temperature T_s. The heating rate is given by

$$Q_r = \frac{g}{c_p p_s}\frac{\partial\left(I^+ - I^-\right)}{\partial \eta}.$$

Since we are considering atmospheres with no condensible component, we take all gases to be well mixed so that q is constant in space and time. The simplest option

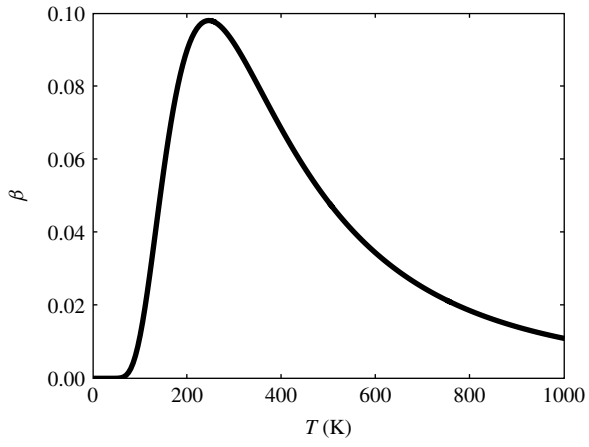

Figure 1. Temperature dependence of β computed with a 2 μm spectral interval centred at 15 μm.

DOI: 10.1002/qj

would be to also take k_b as a constant in space, but in general we expect pressure broadening of absorption lines to make the atmosphere more opaque at lower levels, affecting the static stability and ultimately tropopause height. Again following WR, this effect can be taken crudely into account by including a linear dependence on pressure:

$$k_b = k_{0b}(1 + 2r\,\eta), \tag{13}$$

where k_{0b} is the top-of-atmosphere absorption coefficient while r measures the sensitivity of k_b to pressure. Substituting in (10) yields

$$\tau = \tau_\infty \left(1 - \frac{\eta + r\eta^2}{1 + r}\right), \tag{14}$$

where $\tau_\infty = \beta k_{0b}(1 + r)q\,Dp_s/g$ is the total broadband optical depth of the atmosphere. To simplify matters, in what follows we will only consider two limits: the weak pressure broadening limit $r \to 0$, which gives $\tau = \tau_\infty(1 - \eta)$, and the strong pressure broadening limit $r \to \infty$, which yields $\tau = \tau_\infty(1 - \eta^2)$.

2.3. Surface

The atmosphere is coupled at its lower boundary to a thermodynamic slab of fixed heat capacity. A linearised bulk aerodynamic formulation is used to transfer sensible heat and momentum between the atmosphere and the slab:

$$F_h = c_p\gamma(T_s - T_0), \tag{15}$$

$$F_x = -\gamma u_0, \tag{16}$$

$$F_y = -\gamma v_0, \tag{17}$$

where F_h, F_x and F_y are fluxes of sensible heat, zonal and meridional momentum respectively (defined positive upwards); T_0, u_0 and v_0 are respectively temperature, zonal and meridional velocities near the surface, and the exchange coefficient $\gamma = \rho_0 C_d U$, where ρ_0 is surface density, U is a surface velocity scale taken to be 10 m s^{-1}, and $C_d = 0.0013$ is an adimensional constant. The temperature of the slab T_s evolves according to

$$C\frac{\partial T_s}{\partial t} = S + I_0^- - \sigma T_s^4 - F_h, \tag{18}$$

where C is the slab's heat capacity per unit area, S is the insolation and I_0^- is the downward long-wave flux at the surface.

2.4. Insolation

We consider two idealised insolation profiles (Figure 2). The first is the equatorially symmetric second-order Legendre polynomial commonly used in idealised studies of the Hadley cell:

$$S = S_0\left\{1 - \frac{\Delta_s}{3}\left(3\sin^2\varphi - 1\right)\right\}, \tag{19}$$

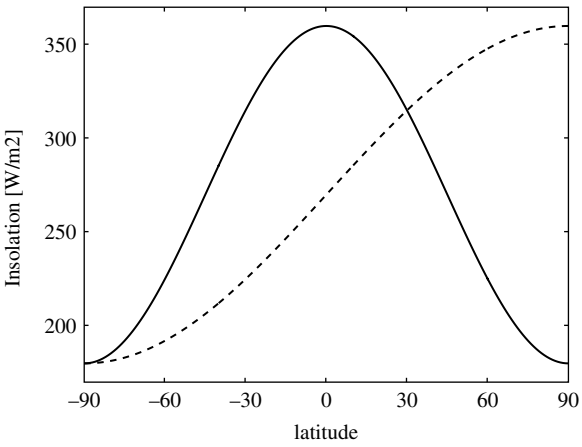

Figure 2. Equatorially symmetric (solid) and antisymmetric (dashed) insolation profiles.

where φ is latitude, S_0 is the global-mean insolation and Δ_s is the fractional Equator-to-Pole drop in insolation. This gives a good fit to annual-average insolation on planets with obliquity greater than about 5°, Δ_s decreasing with increasing obliquity. The second case is antisymmetric around the equator, in an idealization of solstitial conditions:

$$S = S_0\left[1 - \frac{\Delta_s}{3}\left\{3\sin^2\left(\frac{\varphi}{2} - \frac{\pi}{4}\right) - 1\right\}\right], \tag{20}$$

where Δ_s now gives the fractional Pole-to-Pole change in insolation. Surface albedo is taken to be 0; this does not imply a loss of generality, since a non-zero albedo is equivalent to a smaller S_0.

2.5. Numerical solutions: structure of the circulation

Before proceeding to theoretical developments in later sections, it is useful to examine some typical features of the circulation as it appears in a numerical solution of the model outlined above. The equations are discretised on a regular grid with 121 points from Pole to Pole and 30 points in the vertical. For these reference simulations, we take the grey-gas limit ($\beta = 1$) with a total optical depth $\tau_\infty = 1$; this is an arbitrary choice not meant to approximate any particular planetary atmosphere. We use Earth-like values for other parameters: $a = 6370$ km, $\Omega = 2\pi/86400$ s^{-1}, $g = 9.8$ m s^{-2}, $R = 287$ J kg^{-1}K^{-1}, $c_p = 1005.7$ J kg^{-1}K^{-1}, $S_0 = 300$ W m^{-2} and $\Delta_s = 0.6$. The sensitivity of the circulation to these parameters is studied in section 4. For vertical momentum diffusivity we take $\nu = 0.5$ m^{2}s^{-1}. This viscosity will be used in all simulations presented in this paper.

Figure 3 displays results for both the equatorially symmetric (annual mean) and antisymmetric (solstitial) insolation. As is apparent in Figures 3(c, f), potential temperature has been vertically homogenised in the troposphere so isentropes are vertical there. The parameter setting used here puts the radiative-convective equilibrium

DOI: 10.1002/qj

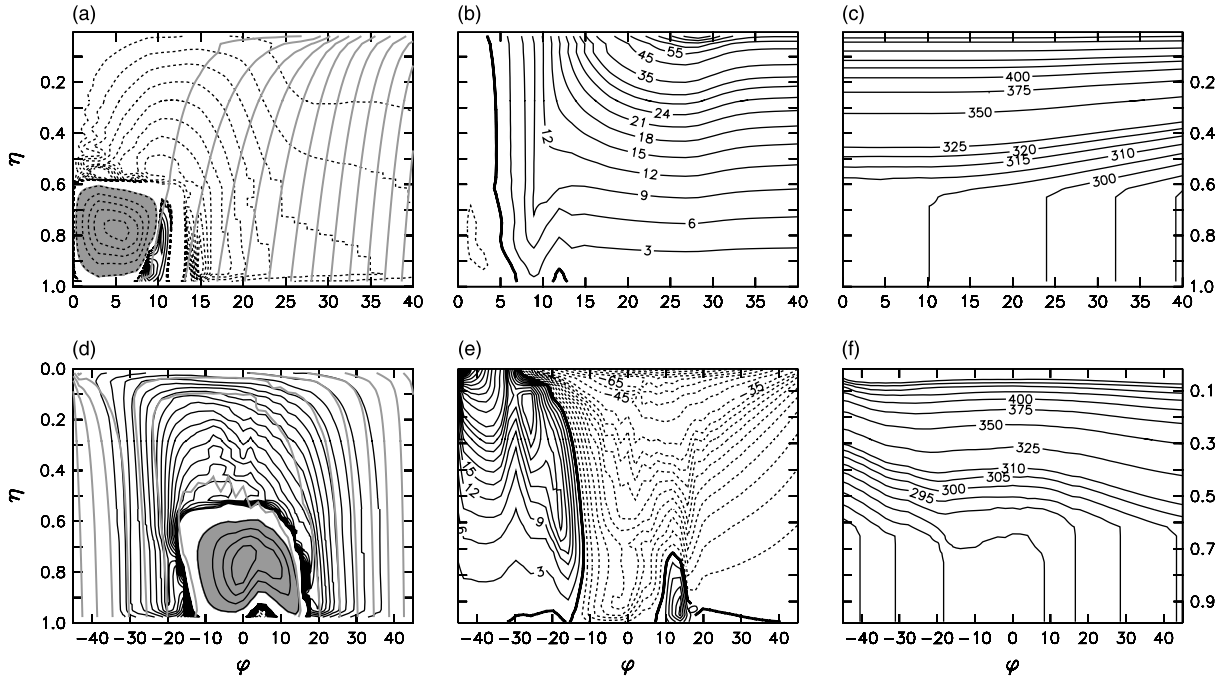

Figure 3. Numerical results (adimensional pressure, η, versus latitude, φ) using the equatorially symmetric or 'annual mean' insolation profile (top row), and the antisymmetric or 'solstitial' profile (bottom row). (a, d) show streamfunction (black contours) and angular momentum (grey contours). Contour interval (CI) for the streamfunction is 0.2 of the maximum value within the area shaded grey, with the outermost contour at 0.1 of the maximum; outside this area, the CI is 0.002 of the maximum. Solid lines indicate anti-clockwise circulation, dashed lines clockwise. Contour interval for angular momentum is 10^8 m^{2}s^{-1} in (a) and 2×10^8 m^2 in (d). (b, e) show zonal wind, CI 5 m s^{-1} for speeds up to 35 m s^{-1}, CI 10 m s^{-1} thereafter, with zero contour bold. (c, f) show potential temperature, CI 5 K from 290 to 325 K, and 25 K thereafter.

tropopause at $\eta_t = 0.61$. The presence of a circulation does not greatly affect the structure or position of the tropopause, which remains essentially horizontal with no break at the poleward margin on the Hadley cell.

There are really two distinct circulations: a narrower, vigorous cell confined to the troposphere, and a broader, much weaker circulation embracing both the troposphere and stratosphere, which we will refer to as the 'deep' cell. It is not surprising to find a circulation also within the stratosphere, given the strong horizontal temperature gradients there. The weakness of the deep cell is due to the large static stability in the stratosphere (section 6). In the annual-mean case, a weak indirect 'Ferrel' cell appears at the poleward margin of the the tropospheric cell, leading to a region of surface westerlies (not shown). A similar feature was found in the least viscous cases studied by HH; as they point out, this arrangement is necessary to balance the convergence of zonal momentum into the descending branch of the Hadley cell by the nonlinear vorticity transport ζv. It is interesting to note the 'jump' in the cross-equatorial low-level return flow of the solstitial case, which has been discussed by Pauluis (2004).

The grey contours in the annual-mean case (Figure 3(a)) show that AM has been entirely homogenised within the tropospheric cell. Streamlines and AM contours cross in the subsiding branch of the deep cell, indicating a significant role for viscosity there. In the solstitial case (Figure 3(d)), AM is again homogeneous within the tropospheric cell; the deep cell shows generally good alignment between streamlines and AM contours, though with some crossing, suggesting an active if weaker role for viscosity than in the annual-mean case.

Figure 4 presents zonal wind profiles in the numerical simulations. Comparison with the 'AM conserving' profiles (dashed lines) shows that AM is conserved to a perhaps surprisingly good approximation at the top of the deep cell in both annual-mean and solstitial cases, with very intense jets appearing at the poleward margin of the Hadley cells. (In Figure 4(b), the jet maximum is actually stronger than the AM-conserving wind based on the equatorial AM; this occurs at a single grid point, and we believe it to be a numerical error due to the very strong lateral shear at this point.) Jet structure at the top of the annual-mean deep cell is very similar to that seen in HH (their Figure 5). As air descends in the subtropical branch of the deep cell, strong shear allows viscosity to play an important role, and the jets become progressively weaker and smoother. Wind profiles within the tropospheric Hadley cell are again close to the AM-conserving limit, with weak but discernible jets at the cell boundary. Further poleward (at around 25° latitude in the annual mean case) there is a secondary, broad wind maximum corresponding to the tropospheric section of the deep cell's subsiding branch.

As discussed in HH, the role of viscosity depends on the ratio of a dynamical time-scale τ_D to a viscous time-scale τ_ν; viscosity should be negligible when $\tau_D/\tau_\nu \ll 1$. The relevant dynamical time-scale in the subsiding branch of the Hadley cell is the time taken to subside

DOI: 10.1002/qj

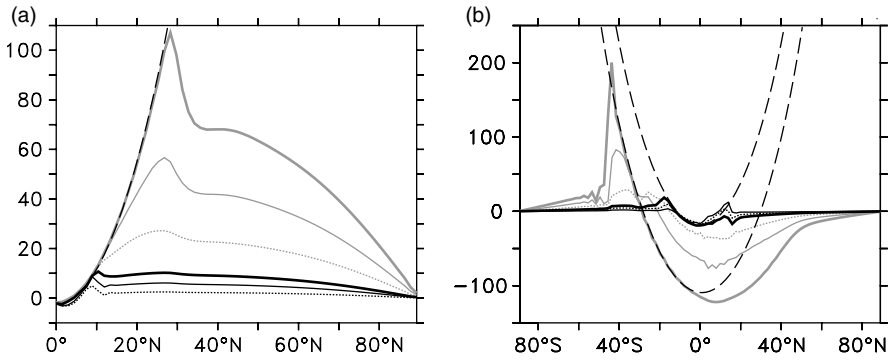

Figure 4. Zonal wind speed (m s^{-1}) in the troposphere (black solid lines) and in the stratosphere (grey lines) for (a) the reference annual-mean run and (b) the reference solstitial run. The wind is plotted at 6 levels: top model level (thick grey), $\eta = 0.1$ (thin solid grey), $\eta = 0.3$ (dotted grey), tropopause (thick black), $\eta = 0.75$ (thin solid black) and $\eta = 0.9$ (dotted black). Dashed lines show zonal wind corresponding to constant angular momentum fixed at the equatorial value.

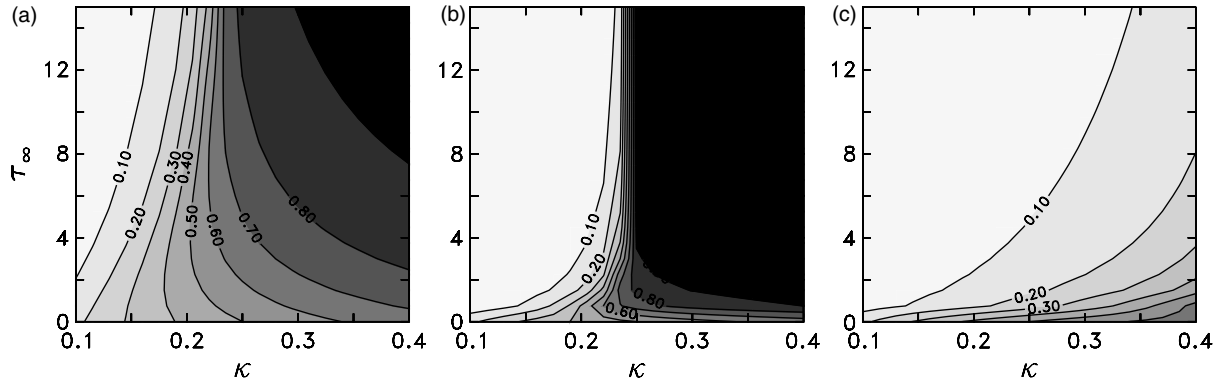

Figure 5. Adimensional tropopause level η_t as a function of κ and τ_∞ assuming (a) $\beta = 1$ and no pressure broadening, (b) $\beta = 0.1$ and no pressure broadening, (c) $\beta = 0.1$ and strong pressure broadening.

through the depth of the cell, which can be estimated directly from the vertical velocities observed in the simulations. For the annual-mean case, we find $\tau_D \sim 10^6$ s for the tropospheric cell and 10^9 s for the deep cell. The corresponding values for the solstitial case are 10^4 and 10^8 s.

Using a simple scaling of the viscous term in the zonal momentum equation (2), we can estimate the viscous time-scale for the bulk of the flow as

$$\tau_\nu \sim \frac{H^2}{\nu}\left(\frac{\Delta\eta}{\eta_0}\right)^2,$$

where H is the pressure scale height, $\Delta\eta$ is the pressure difference across the cell and η_0 is the typical pressure within the cell. For the Earth-like choice of parameters in these runs, the scale height comes to about 8 km. Taking $\Delta\eta/\eta_0 \sim 1$ then gives $\tau_\nu \sim 10^{10}$ s. Thus, $\tau_D/\tau_\nu < 10^{-4}$ for the tropospheric cell in both cases, consistent with AM conservation there. On the other hand, $\tau_D/\tau_\nu \sim 0.1$ for the deep cell of the annual-mean case, in line with a greater role for viscosity there. For the solstitial deep cell, $\tau_D/\tau_\nu \sim 0.01$, suggesting an intermediate role for viscosity in that case.

The above discussion does not account for the AM conservation observed at the model top in both runs. We argue that a more relevant dynamical time-scale here is the time taken to traverse the *horizontal* extent of the cell. Given the cell widths and meridional winds observed in the simulations gives $\tau_D \sim 10^8$ s for the annual-mean case and 10^7 s for the solstitial case. Furthermore, at least in the annual-mean case, much of this time is actually spent in the low-shear zone near the Equator, where viscosity will have less effect. The viscous time-scale will also be different; since we are near the top of the atmosphere, $\eta_0 \ll 1$ (specifically, $\eta = 0.015$ at the midpoint of the top model level), leading to a considerably longer τ_ν than for the bulk of the atmosphere. Overall, these arguments suggest a much smaller value of τ_D/τ_ν near the top of the model than in the bulk of the deep cell.

The circulations shown here are not perfectly steady; the simulations show some amount of transient activity particularly in the troposphere (the figures show averages over the last 1000 days of 3000-day simulations). The heat and momentum transports by these transients could in principle be strong enough to violate the nearly inviscid assumption. On the other hand, HH provide arguments to suggest that the transients should generally play a small role. To assess this question, we have explicitly computed the heat and momentum budgets for the circulation in several model runs; we find in all cases that the

DOI: 10.1002/qj

transient terms are negligible compared with the time-mean terms.

3. Theory for tropopause height

The band-semigrey scheme can be solved in radiative equilibrium (see Appendix) to yield the temperature profile

$$\sigma T^4 = \frac{S(\beta + \tau_\infty - \tau)}{2\beta + (1-\beta)\tau_\infty}, \tag{21}$$

and surface temperature

$$\sigma T_s^4 = \frac{S(2\beta + \tau_\infty)}{2\beta + (1-\beta)\tau_\infty}, \tag{22}$$

which are very similar, if not exactly identical, to WR's (11). WR discuss these solutions in detail, including the effects of pressure broadening, and show that they are considerably more realistic than the grey-gas solutions.

Here, we go a step further and solve for the tropopause level and temperature profile in radiative-convective equilibrium. We do this using the standard approach of matching a convectively adjusted tropospheric temperature profile with fixed lapse rate to a stratospheric profile in radiative equilibrium (Goody and Yung, 1989; Held, 1982; Thuburn and Craig, 2000). Requiring continuity of temperature and upward radiative flux across the tropopause, and assuming that surface temperature T_s equals near-surface temperature T_0, we obtain (see Appendix)

$$\frac{2 + (\tau_\infty - \tau_t)/\beta}{1 + (\tau_\infty - \tau_t)/\beta}\,\eta_t^{4\kappa} = e^{-\tau_t/\beta} + \int_0^{\tau_t/\beta} \eta^{4\kappa} e^{(\tau-\tau_t)/\beta} d\tau/\beta, \tag{23}$$

where subscript t indicates quantities evaluated at the tropopause, and $\kappa = R/c_p$, with R the gas constant and c_p the specific heat capacity. Together with (14), this is an implicit equation for the tropopause level η_t in terms of τ_∞, κ, β and r. (23) assumes the tropospheric lapse rate is dry adiabatic, but it could easily be generalised to an arbitrary lapse rate by replacing $\eta^{4\kappa}$ under the integral with a suitable function of η.

(23) cannot be solved analytically but is readily solved numerically to yield the results shown in Figure 5. Figure 5(a) shows that in the grey limit $\beta = 1$, and ignoring the effects of pressure broadening ($r = 0$), the tropopause rises as τ_∞ increases when $\kappa < 1/4$, while for $\kappa > 1/4$ it approaches the ground. Thus, grey-gas radiative-convective equilibria at large τ_∞ are essentially in only one of two regimes: 'all troposphere', where the entire atmosphere is convectively mixed, and 'all stratosphere', with no convective mixing at all. The two are separated by a sharp transition at $\kappa = 1/4$. Intermediate tropopause elevations are possible only at lower values of τ_∞.

The band-semigrey case (Figure 5(b)) shows these same qualitative features, but with the binary all-troposphere/all-stratosphere region shifted towards lower values of τ_∞. This is because β only enters (23) as a scaling factor of optical path, so that a band-semigrey atmosphere has the same tropopause height as a grey one but with τ_∞ increased by a factor of $1/\beta$. Introducing pressure broadening (Figure 5(c)) destabilises the all-stratosphere equilibria, so that the all-troposphere regime becomes dominant.

(23) also shows that η_t has no dependence on S, so that tropopause level is independent of latitude (in agreement with the flat tropopause seen in the numerical simulations, Figure 3). As a result, the radiative-convective equilibrium potential temperature takes on the separable form

$$\Theta^{rce} = \Theta_0^{rce}(\varphi)\, P(\eta), \tag{24}$$

where Θ_0^{rce} is the vertically uniform tropospheric potential temperature and P is an adimensional vertical profile which is constant in the troposphere and follows radiative equilibrium in the stratosphere. These take the form

$$\Theta_0^{rce} = \left(\frac{S}{\sigma}\right)^{1/4} \left[\frac{1 + (\tau_\infty - \tau_t)/\beta}{2\beta\eta_t^{4\kappa} + (1-\beta)\{1 + (\tau_\infty - \tau_t)/\beta\}}\right]^{1/4}, \tag{25}$$

and

$$P = \begin{cases} 1 & \text{for } \eta > \eta_t, \\ \left(\dfrac{\beta + \tau_\infty - \tau}{\beta + \tau_\infty - \tau_t}\right)^{1/4} \left(\dfrac{\eta}{\eta_t}\right)^{-\kappa} & \text{otherwise.} \end{cases} \tag{26}$$

Both the tropopause level η_t computed from (23) and the separability condition (24) will be used extensively below, so it is worth examining their limits of validity. The predicted tropopause level can be in error because the assumption that surface temperature T_s equals near-surface temperature T_0 cannot really be true, since surface cooling by turbulent heat flux – which feeds convection in the troposphere – requires $T_s - T_0 > 0$. As can be seen from (18),

$$T_s - T_0 = \frac{S + I_0^- - \sigma T_s^4}{c_p \gamma}, \tag{27}$$

so the error will be large for strong insolation, high infrared opacity and weak surface exchange coefficient. Under these conditions, not only will predicted tropopause levels will be in error, but the meridional insolation gradient will induce a significant tropopause slope, and the separability assumption (24) may also fail.

Figure 6 compares numerically simulated tropopause levels with those predicted by (23) over a range of parameter settings. The predictions are quite accurate except for strong insolation. Sensitivity to insolation is shown by the six points in Figure 6 marked with inverted triangles, which correspond to $S_0 = 300$, 1200, 2700, 4800, 24 300 and 76 800 W m^{-2} respectively moving from left to right. Note that the error is not too severe even for $S_0 = 2700$ W m^{-2}, which corresponds roughly to the orbital radius of the solar system's innermost

DOI: 10.1002/qj

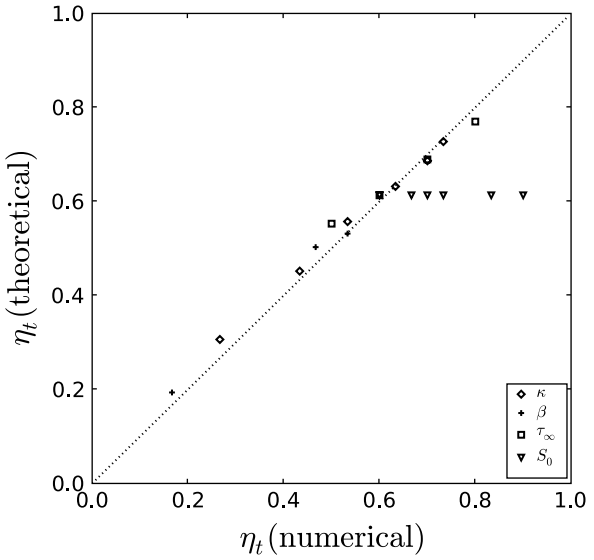

Figure 6. Comparison of tropopause level η_t in numerical simulations with that predicted by (23). The relevant parameters (as indicated by the legend) have been varied over the ranges shown in Table I. S_0 has been varied as discussed in section 3.

planet, Mercury. Note also that these simulations employ $\beta = 1$, and the error would be considerably reduced with the small β values associated with CO_2. On the other hand, a low-density atmosphere such as Mars's will have a weak surface exchange coefficient and the error will be enhanced; however, comparison with Mars GCM results in section 8 suggests that even in this case the error is not too severe. By solving the surface energy balance (18) it would be possible to extend the theory to make the tropopause level predictions more accurate, but we will not pursue this here.

4. Theory for Hadley cell width in the equatorially symmetric case

In the final section of their paper, HH outline how their theory – which employs the Boussinesq approximation and treats diabatic heating using Newtonian cooling – might be extended to a compressible, radiative-convective atmosphere. In this section we flesh out that outline using the radiative-convective results of previous section. We begin by reviewing key results from HH. (29)–(37) below are essentially identical to corresponding equations in HH, and are reproduced here only for the reader's convenience.

As in HH, we assume that the circulation is not strong enough to significantly perturb the vertical temperature structure away from its radiative-convective equilibrium value. This means that the potential temperature retains the separable form

$$\Theta = \Theta_0(\varphi)\, P(\eta), \tag{28}$$

where Θ_0 is the tropospheric potential temperature and P is the radiative-convective equilibrium vertical profile (26).

The first step is to integrate the equation for gradient wind balance

$$\frac{\partial}{\partial \eta}\left(2\Omega \sin\varphi\, u + \frac{\tan\varphi}{a} u^2\right) = \frac{\eta^{\kappa-1} R}{a} \frac{\partial \Theta}{\partial \varphi}, \tag{29}$$

over the depth of the cell. Using assumption (28) and neglecting surface winds, this gives

$$2\Omega \sin\varphi\, u_{\text{top}} + \frac{\tan\varphi}{a} u_{\text{top}}^2 = -\frac{R}{a}\, c_1\, \frac{\partial \Theta_0}{\partial \varphi}, \tag{30}$$

where u_{top} is the cell-top zonal wind and

$$c_1 = \int_{\eta_{\text{top}}}^{1} P\, \eta^{\kappa-1}\, \mathrm{d}\eta, \tag{31}$$

is an adimensional constant.

Assuming that air rises vertically at the Equator, carrying the same AM as the surface, and then moves horizontally poleward along the top of the cell while conserving AM, the cell-top zonal wind can be written

$$u_{\text{top}} = \Omega a\, \frac{\sin^2\varphi}{\cos\varphi}. \tag{32}$$

Substituting this expression in (30) and integrating meridionally gives

$$\Theta_0(\varphi) = \Theta_{00} - \frac{\Omega^2 a^2}{2 c_1 R} \frac{\sin^4\varphi}{\cos^2\varphi}, \tag{33}$$

where Θ_{00} is the value of Θ_0 at the Equator.

Hadley cell width is determined by the twin requirements that (i) the energy budget of the entire Hadley cell is closed, and (ii) the temperature structure (33) matches the radiative-convective equilibrium profile continuously at the cell boundary. In a dry atmosphere, the total flux of dry static energy $\Sigma = c_p T + gz$ across a latitude line can be obtained diagnostically from the top-of-cell radiative imbalance (Peixoto and Oort, 1992):

$$F_h(\varphi) = \frac{2\pi a}{g} \cos\varphi\, \overline{v\Sigma} = 2\pi a^2 \int_0^{\varphi} \Delta(\varphi') \cos\varphi' \mathrm{d}\varphi', \tag{34}$$

where an overbar represents the vertical integral with respect to pressure from the cell top to the ground and

$$\Delta = S - I_{\text{top}}^{+} + I_{\text{top}}^{-}, \tag{35}$$

is the top-of-cell radiative imbalance. Thus, requirements (i) and (ii) above translate respectively into

$$\int_0^{\varphi_{\text{H}}} \Delta(\varphi) \cos\varphi\, \mathrm{d}\varphi = 0, \tag{36}$$

$$\Delta(\varphi_{\text{H}}) = 0, \tag{37}$$

where φ_{H} is the latitude of the cell's poleward boundary. These equations amount to an 'equal area' construction employing top-of-cell radiative fluxes (HH).

DOI: 10.1002/qj

To proceed, we need to relate the cell-top infrared fluxes $I^+_{\rm top}$ and $I^-_{\rm top}$ to the known temperature structure (33). This is straightforward for the upwelling flux if we again make the separability assumption (28), and if we also assume that surface temperature and near-surface atmospheric temperature are close enough that their difference may be neglected. With these two assumptions, we may write

$$I^+_{\rm top} = c_2 \sigma \Theta_0^4, \tag{38}$$

where

$$c_2 = 1 - \beta\left(1 - {\rm e}^{-\tau_{\rm top}/\beta}\right) + \int_0^{\tau_{top}/\beta} P^4 \eta^{4\kappa} {\rm e}^{(\tau-\tau_{\rm top})/\beta} {\rm d}\tau. \tag{39}$$

The cell-top radiative imbalance is then

$$\Delta(\varphi) = S_0\left(1 + \frac{\Delta_s}{3}\right) + I^-_{\rm top} - \Delta_s \sin^2\varphi - c_2\sigma\left(\Theta_{00} - \frac{\Omega^2 a^2}{2c_1 R}\frac{\sin^4\varphi}{\cos^2\varphi}\right)^4. \tag{40}$$

For the deep cell, $I^-_{\rm top}$ is zero. Substituting (40) into (36)–(37) then gives two equations in the two unknowns Θ_{00} and $\varphi_{\rm H}$. The equations can be solved numerically using a root-finding algorithm.

The tropospheric case is more complicated, since $I^-_{\rm top}$ is then the downwelling flux from the stratosphere; one should first solve for the deep circulation, and use the temperature structure thus found to compute $I^-_{\rm top}$. In practice, this step can be avoided by making some further simplifying approximations. Note firstly that the deep cell is always much wider than the tropospheric cell; as a result, there is almost no meridional temperature gradient in the stratosphere above the tropospheric cell (Figure 3c, f)), and $I^-_{\rm top}$ can be taken to be constant. This assumption implies that $I^-_{\rm top}$ does not affect the geometry of the equal-area construction, and thus does not affect Hadley cell width, though it does affect Θ_{00}. However, Θ_{00} is in fact always quite close to the radiative-convective equilibrium value; in numerical simulations spanning a broad parameter range, we found that Θ_{00} did not deviate from $\Theta^{\rm rce}_{00}$ by more than a few percent, even for parameter settings that produce a wide tropospheric cell. Thus, in the tropospheric case we set $\Theta_{00} = \Theta^{\rm rce}_{00}$ and solve (36)–(37) for $\varphi_{\rm H}$ and $I^-_{\rm top}$.

Further insight is possible by using the small-angle approximation, so that (40) takes the form

$$\Delta(\varphi) \approx \Delta_0 - S_0\Delta_{\rm s}\varphi^2 + \sigma\Theta_{00}^3\frac{2c_2\Omega^2a^2}{c_1R}\varphi^4, \tag{41}$$

where Δ_0 is the radiative imbalance at the Equator. (36)–(37) can then be solved analytically to give

$$\varphi_{\rm H} = \left(\frac{5}{3}\,A\,Ro\right)^{1/2}, \tag{42}$$

$$\text{where} \quad Ro = \frac{RT_e\Delta_s}{\Omega^2a^2}, \tag{43}$$

$$\textit{and} \quad A = \frac{1}{4}\frac{c_1}{c_2}\left(\frac{T_{\rm e}}{\Theta^{\rm rce}_{00}}\right)^3, \tag{44}$$

and we have introduced the characteristic temperature

$$T_{\rm e} = \left(\frac{S_0}{\sigma}\right)^{1/4}. \tag{45}$$

An expression for $\Theta^{\rm rce}_{00}$ can be derived from (25), which shows that A depends on τ_∞, β and κ and only very weakly on Δ_s. Thus A and Ro are essentially independent, with A containing all dependence on radiative-convective parameters and Ro (a thermal Rossby number) containing dependence on 'dynamical' parameters. Note the absence of g in Ro.

Figure 7 compares the theory with the results of numerical simulations spanning a broad parameter range. The parameters and their corresponding ranges are listed in Table I. As is apparent from the figure, the theory is quite accurate over the entire range. The small-angle approximation (dotted lines) fails at widths greater than about 30°, but solutions retaining full trigonometry (solid lines) are accurate even for the widest cells.

5. Connection with Held and Hou's result

(42) can be re-written in a form that clarifies the connection with HH's Boussinesq, Newtonian cooling result (1). Noting that tropopause height within the Hadley cell is to a good approximation given by

$$H_{\rm t} = c_1\frac{R\Theta^{\rm rce}_{00}}{g}, \tag{46}$$

we obtain

$$\varphi_{\rm H} = f\left(\frac{5}{3}\,\frac{gH_{\rm t}\Delta_H}{\Omega^2a^2}\right)^{1/2}, \tag{47}$$

which makes it clear that our result is in fact identical to HH's aside from the factor

$$f = \left(\frac{T_{\rm e}^4}{c_2(\Theta^{\rm rce}_{00})^4}\frac{\Delta_s}{4\Delta_{\rm H}}\right)^{1/2}. \tag{48}$$

Recall that $\Delta_{\rm s}$ is the fractional Equator–Pole drop in insolation, while $\Delta_{\rm H}$ is the corresponding drop in radiative-convective equilibrium temperature. Since $\Theta^{\rm rce}_0 \propto S^{1/4}$ (25), it can be shown that $\Delta_{\rm s}/4\Delta_{\rm H} \approx 1$. Further, $T_{\rm e}^4/c_2(\Theta^{\rm rce}_{00})^4$ is the ratio between upward long-wave flux at the top of the atmosphere and at the tropopause. Overall, we expect $f < 1$, so that (47) predicts a smaller cell width for a given cell height than HH's formula (1).

DOI: 10.1002/qj

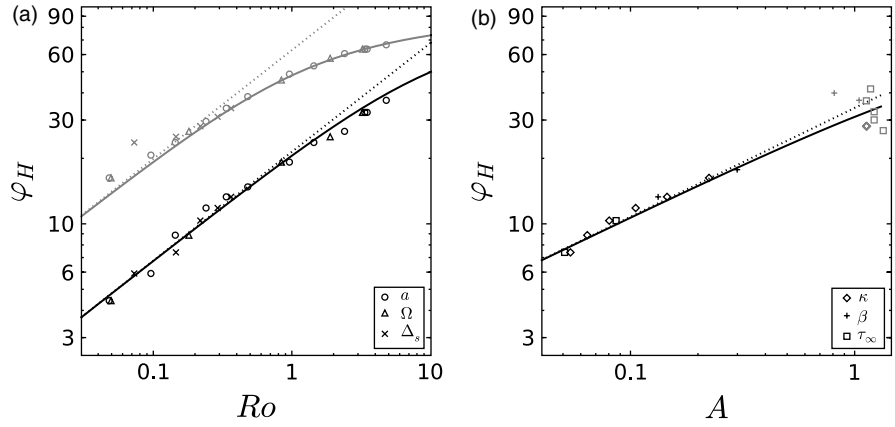

Figure 7. Sensitivity of Hadley cell width φ_H to adimensional parameters (a) Ro and (b) A in the equatorially symmetric case. Black lines and symbols refer to the tropospheric cell, grey to the deep cell. Symbols show results from numerical simulations. In each simulation, a different dimensional parameter – as indicated by the legend in each panel – was varied away from the reference value specified in Table I. Hadley cell width in the simulations is estimated from the position of the jet maximum at cell top. The jet maximum is measured as the latitude of the grid point at which zonal wind reaches its first maximum starting from the Equator. 'Cell top' for the deep cell is taken as the top model layer, and for the tropospheric cell as the model layer containing the radiative-convective equilibrium tropopause η_t. Dotted lines show the theoretical estimate of φ_H using the small-angle approximation, given by (42). Solid lines show the estimate of φ_H without the small-angle approximation, obtained by numerically solving (36)–(37) using (40). In both estimates, the top of the deep cell is taken as the midpoint of the top model layer, $\eta = 0.015$, while the top of the tropospheric cell is taken to be at $\eta = \eta_t$. In (a), A is held constant at 0.09 for the tropospheric cell and 0.61 for the deep cell. In (b), $Ro = 0.22$.

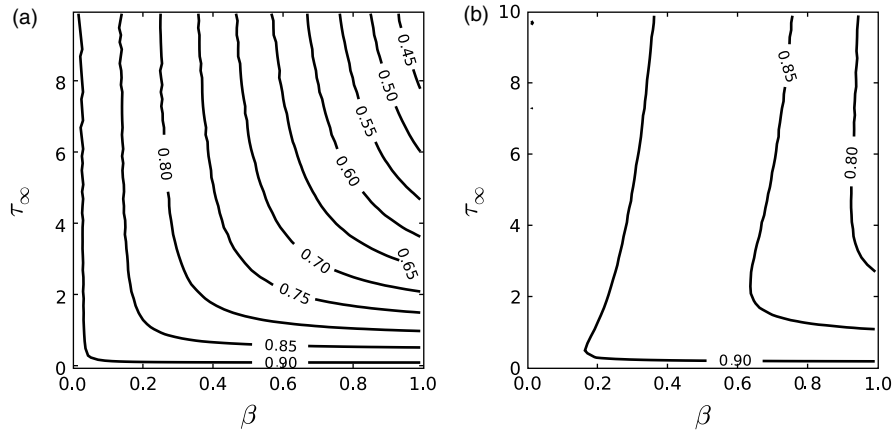

Figure 8. Values of f, the ratio of Hadley cell width predicted by the present theory and by HH, for $\kappa = 2/7$ in the case of (a) no pressure broadening and (b) strong pressure broadening.

Table I. Parameter ranges spanned by numerical simulations. Range bounds are expressed as multiples of the reference value.

Parameter	Meaning	Unit	Reference value	Range
a	Planetary radius	m	6.37×10^6	0.25–3
Ω	Rotation rate	s^{-1}	$2\pi/86400$	0.25–3
Δ_s	Equator–Pole insolation drop	–	0.6	0.33–1.66
τ_∞	Optical depth	–	1	0.1–20
κ	R/c_p	–	2/7	0.7–2
β	Bandwidth	–	1	0.05–1

The difference will be large only for atmospheres with an optically thick stratosphere.

The parameter dependence of f is presented in Figure 8. As expected, f is close to 1 for small τ_∞ and β, which give optically thin atmospheres. f is close to 1 even for large τ_∞ and β when pressure broadening is strong, which gives a high tropopause (Figure 5) and thus a thin stratosphere.

A direct comparison between theory and numerical results is presented in Figure 9. Grey dots compare cell width in numerical simulations with that predicted by solving HH's equations (13a, 13b), which use the Boussinesq and Newtonian cooling assumptions, setting cell height equal to the radiative-convective tropopause height (46) and taking $\Delta_H = \Delta_s/4$. (We have checked this latter approximation to be accurate to better than 7%.) The exact solution is shown, without recourse to the small-angle approximation. The black dots show solutions to our (36)–(37) using (40), again without making the small-angle approximation. The difference between the two estimates, visualised by the length of the vertical lines in Figure 9, is generally small, particularly

DOI: 10.1002/qj

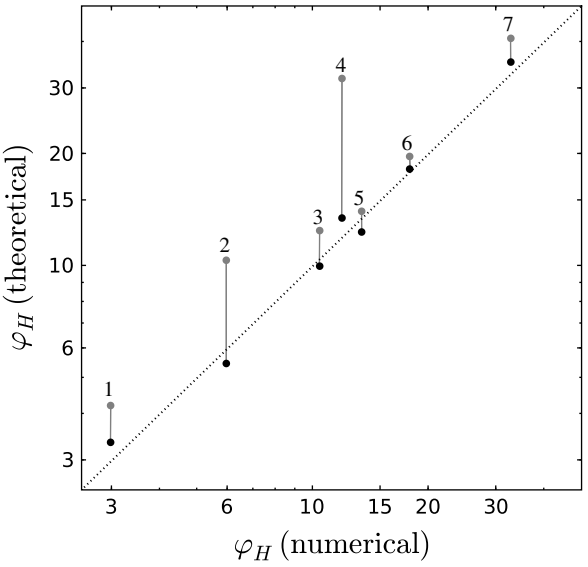

Figure 9. Comparison between tropospheric Hadley cell width in numerical simulations and theoretical predictions. The comparison is performed for 7 cases, each represented in the figure by two dots joined by a vertical line and identified by a number. For each case, the upper (grey) dot shows the width estimated by solving the exact equal-area equations using the Newtonian cooling approximation as in HH, while the lower (black) dot shows our radiative-convective estimate (see text for further details on how the theoretical estimates are obtained). Numerical cell widths are estimated as detailed in Figure 7. For each case, numerical values are plotted along the abcissa and theoretical values along the ordinate; the dashed line indicates a perfect match. Case 3 employs the default parameter setting (Table I), while other cases use: (1) $a = 3a_0$, where a_0 is the default planetary radius, (2) $\tau_\infty = 5$, (4) $a = a_0/4$, $\tau_\infty = 10$, (5) $\beta = 0.5$, (6) $\beta = 0.05$, and (7) $a = a_0/3$.

in cases 5 and 6 which use small β. In cases 1, 3, 5, 6 and 7 our radiative-convective theory cannot be said to do an unambiguously better job at predicting the numerical cell width than HH. Several effects contribute towards a mismatch between theory and simulations: the role of non-zero viscosity in the simulations, the use of the the approximation $\Theta_{00} = \Theta_{00}^{\rm rce}$, uncertainty in the exact value of $H_{\rm t}$, and failure of the separability assumption (28). Another difference between the radiative-convective case and Newtonian cooling is that the radiative relaxation rate in the former is spatially varying, while it is constant in the latter; however, this is more likely to affect the strength rather than the width of the cell. Overall, it seems safe to conclude that the difference between the two theories is comparable to the difference between either theory and the numerical results, making the two theories empirically indistinguishable in these cases.

We have also included two cases (2 and 4) in which the difference between the two theories is greater. The parameter settings in these two cases are $\tau_\infty = 5$ and 10 respectively, $\beta = 1$ and $r = 0$ (no pressure broadening). These parameter settings give low tropopause levels ($\eta_{\rm t} = 0.77$ and 0.85 respectively), so roughly 80% of atmospheric mass is in the stratosphere which is thus optically thick. Figure 8(a) shows that $f \approx 0.5$ under these conditions. Consistently, the present theory predicts a cell width about half as large as HH in these two cases, and is in better agreement with the numerical results. Perhaps the greatest uncertainty in the comparison between theory and simulation is in the choice of cell height; it may be argued that if the poleward flow is not tightly concentrated near the tropopause but occurs over a broad layer, as it does in our simulations, then one should use an effective height $H_{\rm mf}$ corresponding to the mean mass flux, which would be lower than $H_{\rm t}$ and bring HH's prediction closer to the numerical results. However, even the extreme assumption that the mean mass flux is in the mid-troposphere, $H_{\rm mf} = 0.5H_t$, gives a correction to the cell width of only $\sqrt{0.5} = 0.7$, i.e. a 30% reduction, which is still far from the 50% reduction required to bring HH's estimate into line with the numerical results in cases 2 and 4 of Figure 9.

As shown in Figure 8, small f requires $\beta \approx 1$, $\tau_\infty \gg 1$ and weak pressure broadening. These conditions will rarely be simultaneously satisfied. By and large, atmospheric gases have simple molecular structures and their absorption spectra are generally concentrated in fairly narrow bands, leading to small β. Moreover, large τ_∞ generally requires a considerable mass of the gas to be present, which will typically lead to pressure broadening (however, on a planet with small surface gravity may be able to accommodate large mass with relatively small surface pressure). Thus, small f requires a gas with a very broad absorption spectrum which is also a strong enough absorber to give large optical depth in small concentrations; it is difficult to think of examples of such a gas which, in addition, does not condense. Nonetheless, small f remains at least a theoretical possibility which is worth pointing out. However, we emphasise that cases presenting a large divergence between HH's formula and ours occupy a small region of parameter space; over most of parameter space, our result is essentially indistinguishable from HH's.

6. Energy transport and mass flux

Solving (36)–(37) for Δ_0 with the small angle approximation yields

$$\Delta_0 = \frac{1}{6} S_0 \Delta_{\rm s} \varphi_{\rm H}^2 = \frac{5}{18} S_0 \Delta_{\rm s} ARo. \tag{49}$$

Substituting into (41) and integrating meridionally, the energy transport (34) can be explicitly determined. The maximum transport occurs at $\varphi^2 = ARo/3$, and has the value

$$F_{\max} = \frac{\pi}{5^{3/2}} a^2 S_0 \Delta_{\rm s} \varphi_{\rm H}^3 = \frac{\pi}{3^{3/2}} a^2 S_0 \Delta_{\rm s} (ARo)^{3/2}. \tag{50}$$

Thus, for any given cell width the energy flux simply scales with the solar forcing gradient. The Rossby number and optical thickness affect the maximum flux only through the width of the cell; a wider cell means that more net solar energy must be transported from one

DOI: 10.1002/qj

place to another. In particular, the optical thickness of the atmosphere has only a weak effect on the heat flux, via the parameter A which enters into the determination of the cell width. Thus, for a dry planet in which static stability is unaffected by the circulation, warming the atmosphere by increasing its greenhouse effect alters the heat flux only insofar as the increased greenhouse effect makes the Hadley cell wider or narrower.

Figures 10(a, b) compare the predicted scaling of Δ_0 and heat flux against numerical results. In the simulations, the heat flux is measured by meridionally integrating the top-of-cell radiative imbalance, using the second equality in (34) – what is sometimes called the 'implied' heat flux. The energy budget of the tropospheric cell is not in fact closed, because this cell is embedded in the larger deep cell, and there is some advective heat transport through the boundaries. The transport term through the top of the cell has little meridional structure, however, and can be approximately removed by subtracting the cell-mean imbalance before integrating meridionally. The figure shows generally good agreement between theory and simulations for both the tropospheric and deep cell.

The heat flux scaling tells us how much heat the Hadley cell must transport, but it does not give us much of an inkling as to how the circulation actually accomplishes the required transport. Indeed, it is not clear how the tropospheric cell can transport heat at all, since dry convection relaxes the troposphere to a state of constant Θ, which is also a state of constant dry static energy Σ since $\mathrm{d}\Sigma = c_p T\,\mathrm{d}(\ln\Theta)$. The answer, as shown in Figure 11, is that the cell generates its own static stability through two mechanisms. Firstly, the cell's poleward branch homogenises upper-tropospheric potential temperature to the equatorial value, thereby generating some static stability in the subsiding branch. Secondly, the cell penetrates some way into the stratosphere and advects potentially warmer stratospheric air into the top of the tropospheric subsiding branch, adding to the static stability there.

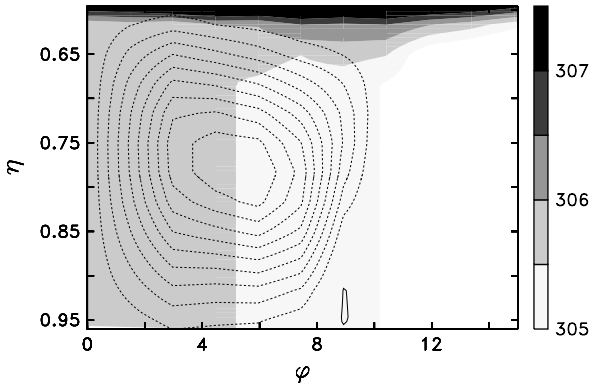

Figure 11. Close-up of the tropospheric cell in the equatorially symmetric reference run (Figure 3(a)), showing streamfunction (contours, interval 0.1 of maximum value) and potential temperature (shading, interval 0.5 K).

If $\Delta\Sigma$ is the dry static energy difference between the bottom and top of the cell, then the mass flux carried by the circulation is

$$V \sim \frac{F_{\max}}{\Delta\Sigma} \sim \frac{\pi a^2 S_0 \Delta_s \varphi_H^3}{5^{3/2} c_p T\, \Delta \ln\Theta}, \tag{51}$$

where we have used (50) and T is a reference temperature. Thus, if $\Delta\ln\Theta$ is independent of cell width, V should scale like φ_H^3. The behaviour of V in the numerical results is shown in Figure 10(c). Note that, as mentioned in section 2.5, the tropospheric cell is much stronger than the deep cell: for a given φ_H, both cells have the same heat flux (Figure 10(b)), but the deep cell has much greater $\Delta\Sigma$ so a much weaker mass flux is required. The deep cell's mass flux scales as φ^3 throughout, implying that the mass flux is in all cases too weak to modify the static stability set by the radiative-convective equilibrium. For the tropospheric cell, the φ_H^3 scaling holds up to $\varphi_H \approx 20^\circ$ but appears to break down thereafter, suggesting that beyond a certain threshold the mass flux

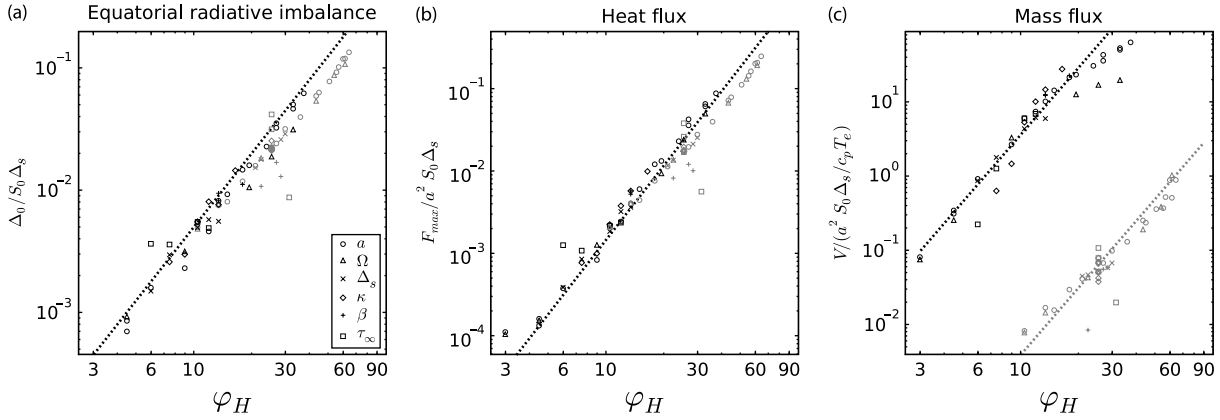

Figure 10. Numerical results for (a) adimensional radiative imbalance at the Equator, $\Delta_0/(S_0\Delta_s)$, with the dotted line showing the theoretical prediction $\varphi_H^2/6$; (b) adimensional energy transport $F_{\max}/(a^2 S_0\Delta_s)$, computed by meridionally integrating the cell-top radiative imbalance according to the second equality in (34), with cell top defined as in Figure 7, and the dotted line showing the theoretical prediction $\pi\varphi_H^3/5^{3/2}$; (c) adimensional mass flux $V/(a^2 S_0\Delta_s/c_p T_e)$, where $T_e = (S_0/\sigma)^{1/4}$, computed as the maximum value of the mass streamfunction, with dotted lines proportional to φ_H^3, and solid line proportional to φ_H. Black lines and symbols refer to the tropospheric cell, grey to the deep cell.

DOI: 10.1002/qj

is strong enough to significantly modify the background temperature structure.

6.1. The optically thin limit

If the temperature of the tropics were horizontally uniform, then the air parcels circulating in the Hadley cell would ascend and descend along the same trajectory in temperature-entropy space, and therefore could do no work. In this case, the circulation must cease, since work must be done to offset frictional dissipation of kinetic energy in the boundary layer. This situation arises in the optically thin limit, $\tau_\infty \to 0$. In this limit, the atmosphere cannot lose entropy radiatively in the subsiding branch. Entropy is then homogenised in the interior, though conduction from the surface maintains an entropy gradient in a shallow boundary layer.

The optically thin limit can be seen as a manifestation of Sandström's result (Sandström, 1908; Defant, 1961) that a fluid whose sources and sinks of heat (or entropy) are at the same pressure can do no work, so all motion must cease. (See also Paparella and Young (2002) and chapter 15 of Vallis (2006) for an alternative derivation of a similar result.) Numerical simulations employing very small τ_∞ show that the atmosphere slowly fills with air of potential temperature equal to the warmest surface temperature until all gradients in the interior are wiped out and motion ceases, aside from a very shallow circulation driven by the small amount of thermal diffusion from the ground (analogously, in the oceanic context where Sandström's work originated, the basin fills with the coldest, densest water). As the infrared optical depth increases, the emission level lifts off the ground; the resulting pressure difference between heat source and sink permits a deep, vigorous circulation to exist.

7. Width theory for solstitial insolation

As shown in Figure 3(d), the antisymmetric insolation profile produces a single cell with ascent in the summer hemisphere and descent in the winter hemisphere. Assuming once more that air rises vertically to the top of the cell and then moves horizontally to the subsiding branch, all the while carrying the surface value of AM, cell-top zonal wind is given by

$$u_{\text{top}} = \Omega a \, \frac{\cos^2\varphi_1 - \cos^2\varphi}{\cos\varphi}, \tag{52}$$

(Lindzen and Hou, 1988), where φ_1 is the central latitude of the rising branch. It is then possible to perform an equal-area construction using energy constraints analogous to the equatorially symmetric case and solve for φ_1 and φ_{H} (the poleward boundary of the descending branch) as described in Lindzen and Hou (1988), with the difference that here only a single, cross-equatorial cell forms since the maximum of our insolation profile is directly at the summer pole.

However, this procedure leads to a large overestimate of Hadley cell width. The discrepancy can be understood qualitatively with the following argument. Near the Equator, the solstitial insolation profile (20) is linear in φ with slope Δ_s. Since directly at the Equator the upwelling infrared flux at the cell-top boundary, I^+_{top}, is less than or equal to the insolation at the Equator, the slope of I^+_{top} must exceed the slope of the insolation profile in the summer hemisphere. The theory accomplishes this slope condition by a sharp, vertical updraught reaching to the tropopause, which creates a discontinuity in I^+_{top} at the latitude of the updraught, φ_1. The simulations do not have a sharp, vertical updraught; rather air rises in an arc-like trajectory from the surface at φ_1 to the top of the cell at the Equator. Thus, the assumption that (52) is the zonal wind at the tropopause is violated in the summer hemisphere. (Lindzen and Hou (1988) provide additional discussion of this point.) The simulated I^+_{top} is no longer equatorially symmetric, which allows energy balance in the cell to be achieved. However, (52) holds in the winter hemisphere, and with additional assumptions this fact can be used to construct a scaling law for the width of the cell.

Detailed examination of a range of numerical simulations suggests a more accurate construction based on the following assumptions: (i) air parcels near the top of the cell move horizontally in the winter hemisphere, from the equator to φ_{H}; (ii) $|\varphi_1| \approx \alpha|\varphi_{\text{H}}|$, where α is a constant independent of any planetary parameters; (iii) the circulation transports heat from the summer to the winter hemispheres with no convergence at the equator, so that the temperature there remains near radiative-convective equilibrium. We do not have any fundamental justification for these assumptions, whose motivation is entirely empirical. They hold robustly in numerical integrations spanning a broad region of parameter space.

Assumption (i) allow us to use the wind profile (52) and the gradient wind equation (29) to obtain the winter-hemisphere temperature profile

$$\Theta_0(\varphi) = \Theta_{00} - \frac{\Omega^2 a^2}{2c_1 R}\left\{\left(\frac{\sin^2\varphi - \sin^2\varphi_1}{\cos\varphi}\right)^2 - \sin^4\varphi_1\right\}, \tag{53}$$

which using the small-angle approximation gives

$$I^+_{\text{top}} \approx c_2\sigma\left\{\Theta_{00}^4 - 2\Theta_{00}^3\frac{\Omega^2 a^2}{c_1 R}(\varphi^4 - 2\varphi_1^2\varphi^2)\right\}. \tag{54}$$

Expanding the insolation profile (20) to first order around the Equator,

$$S \approx S_0 + \frac{S_0\Delta_{\text{s}}}{2}\varphi, \tag{55}$$

imposing radiative-convective equilibrium at φ_{H} and using assumptions (ii) and (iii) then gives

$$\varphi_{\text{H}} = -(c\,A\,Ro)^{1/3}, \tag{56}$$

DOI: 10.1002/qj

where Ro and A are defined by (43) and (44) as before, while c is a function of α. Note that φ_H is negative here because we have chosen the insolation maximum to be in the Northern Hemisphere.

Thus, Hadley cell width in the antisymmetric case is controlled by the same two adimensional parameters as in the symmetric case, but this time with exponent 1/3 rather than 1/2. The reason for this difference is geometric: in the symmetric case, the equal-area construction matches a quartic to a quadratic (41), while in the antisymmetric case the construction matches the quartic (54) to the linear function (55). The prediction of 1/3-power law scaling is robustly borne out by comparison with numerical simulations in Figure 12. We lack a theoretical constraint to fix the value of α and therefore of c, which must be inferred empirically by optimizing the fit to numerical simulations. The important point is that c is a 'universal' constant, independent of model parameters (though a different value of c is required for tropospheric and deep cells). Since c only depends on the structure of the circulation, the implication is that cell structure is invariant to changes in cell width and depth.

The insolation in the antisymmetric case is meant to approximate solstice conditions. Our derivation assumes that the surface has low thermal inertia, so that the surface energy budget comes into balance and all solar radiation absorbed at the surface is instantaneously converted to upward turbulent and radiative fluxes. This assumption is appropriate to Mars and Snowball Earth, but in the open water of the Earth's present tropics, the thermal inertia of the ocean would considerably mute the seasonal cycle of the Hadley circulation.

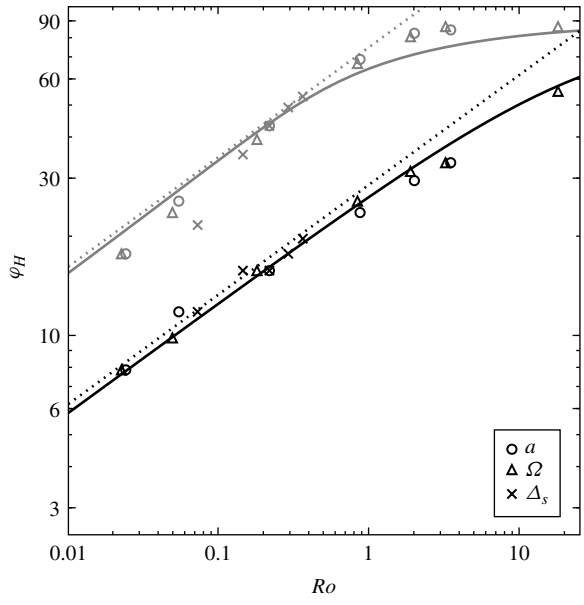

Figure 12. As Figure 7(a), but for the equatorially antisymmetric case. To optimise the fit, the value of α has been arbitrarily set to 2/5 for the tropospheric cell (with $A = 0.13$) and 3/5 for the deep cell (with $A = 0.92$).

8. Application to Mars and Snowball Earth

As an illustration of the theory presented above, we compare it here with previously published simulations of dry planetary atmospheres using 3-dimensional GCMs with more sophisticated radiative transfer schemes and sub-gridscale parametrisation. As pointed out in the Introduction, our axisymmetric theory is at best an incomplete account of the general circulation, since asymmetric eddies are missing as are other confounding issues (the radiative effect of dust in Mars's atmosphere being an example). Thus, comparisons such as those presented below should be viewed with great caution: major discrepancies between theory and simulations will point to inadequacies of the theory's underlying assumptions, while close agreement could be purely coincidental and should not be viewed as proving the theory's validity.

The first example we consider is present-day Mars, which has an atmosphere consisting of 95% CO_2, the remainder being mostly N_2. Surface pressure is only 610 Pa (6.1 mb), and maximum surface temperatures are around 250 K. Observations show a well-mixed dry-adiabatic surface layer some 10 km deep, which crosses over to more stable stratification above 200 Pa (Leovy, 2001). Numerous GCM studies of the Martian circulation exist in the literature (e.g. Barnes and Haberle, 1996; Forget *et al*., 1999; Lewis, 2003). At equinox, the mass streamfunction has a somewhat complex structure, but we may discern in each hemisphere an intense shallow cell filling the convectively-mixed layer with a width of some 20°–30°, embedded in a weaker, broader circulation which is evanescent in height but reaches up to at least the 1 Pa level; this deeper cell has a width of some 40°–50°. During solstice, the circulation has a simpler structure: as in our axisymmetric simulations (Figure 3(d)), there is a single cross-equatorial circulation with an arc-like rising branch and a much more vertical subsiding branch. The poleward margins of the rising and subsiding branches are roughly equidistant from the Equator. There is again an intense, shallow cell with $\varphi_H \approx 15$–$20°$, and a weaker deep cell with $\varphi_H \approx 50$–$60°$.

For the theoretical estimate, we use the following parameters: $a = 3.396 \times 10^6$ m; $\Omega = 7.088 \times 10^{-5}\text{s}^{-1}$; $\kappa = 0.19$, appropriate for a pure CO_2 atmosphere; $S_0 = 70$ W m^{-2}, which takes into account a planetary albedo of 0.25; $\Delta_s = 1$, since at equinox the insolation at the pole is zero; $\tau_\infty = 0.1$ and $\beta = 0.05$, a reasonable choice for the 15 μm CO_2 absorption band at Martian temperatures (Figure 1). We assume weak pressure broadening ($r = 0$), given the low surface pressure. These parameter values yield $\eta_t = 0.44$, which puts the top of the convectively mixed troposphere at 270 Pa, in rough agreement with observations (use of the strong pressure broadening limit puts the top of the troposphere at 180 Pa, also in rough agreement with observations). For this parameter setting, $Ro = 0.62$ and $A = 0.16$ for the tropospheric cell, while $A = 0.93$ for the deep cell. The corresponding widths (which can be read off from Figure 7(a), allowing for the different value of A) are about 20° for the

DOI: 10.1002/qj

tropospheric cell and 45° for the deep cell, giving a reasonable match to the shallow and deep cells identified in the GCM results. Using the same adimensional parameter values and Figure 12, we can also predict cell widths for the solstitial case; we find $\varphi_H \approx 20°$ for the tropospheric cell and 60° for the deep cell, again in agreement with the GCM. We conclude, overall, that in present Mars the troposphere is very shallow and the circulation is dominated by the deep cell: it is for this reason, and because of the planet's smaller radius, that the Hadley cell on Mars appears so much wider than on Earth.

The Hadley cell mass flux on present Mars under equinoctial conditions can be estimated by reading off from Figure 10(c) the adimensional mass flux and multiplying by $a^2 S_0 \Delta_s / c_p T_e \approx 4 \times 10^9$ kg s^{-1}. For a deep cell of 45° width this gives $V \approx 2 \times 10^9$ kg s^{-1}, which is somewhat greater than the $0.5–1 \times 10^9$ kg s^{-1} shown by GCM simulations (Barnes and Haberle, 1996; Forget *et al*. 1999; Lewis 2003). For the tropospheric cell, taking its width to be 20° gives a theoretical mass flux of 120×10^9 kg s^{-1}, which vastly overestimates the $\sim 1 \times 10^9$ kg s^{-1} seen in the GCMs. This large difference most likely points to the effect of large-scale eddies, whose vertical heat transport will significantly increase the static stability in the troposphere (Schneider, 2004) leading to a reduced overturning mass flux.

The second case we consider is 'hard' Snowball Earth, the completely ice-covered state thought to have existed about 750 million years ago during the Neoproterozoic (Hoffman *et al*., 1998). A detailed GCM study of this climatic state (Pierrehumbert, 2005) shows that the high albedo yields tropical surface temperatures below 250 K; at these temperatures the hydrological cycle is very weak, the effects of latent heat release are negligible and CO_2 is the dominant absorber. At equinox, the GCM produces twin tropospheric Hadley cells with a poleward margin around 20° latitude and a cell top between 300 and 400 hPa (Pierrehumbert, 2005, Figure 9). Because ozone is present in the stratosphere of these simulations, we do not expect our theory to apply to the deep cell and will not consider it here. In the rising branch of the tropospheric cell, the temperature follows the dry adiabat up to about 400 hPa, so we may identify these cells as tropospheric cells. At solstice, the model produces a single cell which is roughly symmetric around the Equator and has $\varphi_H \approx 20°$. We compare with theoretical values computed using the following parameters: $S_0 = 130$ W m^{-2}, which takes into account the mean albedo of 0.6 used in the GCM simulations; $\Delta_s = 1$; $\tau_\infty = 0.3$, estimated using a spectrally resolved radiative transfer code with 100 ppm CO_2; and $\beta = 0.05$. We also assume strong pressure broadening, which is reasonable given the 1000 hPa surface pressure. Other parameters have the same values used for the reference case in section 2.5. For these parameter values, $\eta_t = 0.35$, which puts the tropopause at 350 hPa, in good agreement with the GCM. Furthermore, $Ro = 0.29$ and $A = 0.18$ for the tropospheric cell, which gives $\varphi_H \approx 20°$ at both equinox and solstice, again in agreement with the GCM. This agreement may be fortuitous, however; numerical results by Walker and Schneider (2006) using an eddy-resolving model with dry adiabatic background stratification show that Hadley cell width in fact asymptotes to about 20° as tropopause height and insolation gradient increase.

Applying to Snowball Earth the same scaling argument as discussed for Mars, this time for a tropospheric cell 20° wide, gives an equinox mass flux of about 240×10^9 kg s^{-1}, overestimating the GCM's 100×10^9 kg s^{-1} (Figure 9 of Pierrehumbert, 2005). This again points to eddy effects the overestimate here is less severe than for the Martian troposphere; the reason for this difference is unclear to us. As atmospheric CO_2 concentration increases, we expect both τ_∞ and β to increase. These have opposite effects on cell width; a tenfold increase in τ_∞ increases the theoretical width to 23°, while a tenfold increase in β reduces the width to 14°. We thus expect φ_H to be fairly insensitive to CO_2. The same should be true for heat transport and mass flux, which in the present theory depend only on width. The GCM simulations indeed show the mass flux to be nearly independent of CO_2 up to concentrations of 12 800 ppmv (Table 2 of Pierrehumbert, 2005). However, the circulation strength increases rather sharply as CO_2 increases further to 0.2 bar, and neither our scaling theory nor our steady eddy-free simulations account for this behaviour. Another aspect of the GCM simulations that is quite different from the behaviour reported in the present work is that substantial low-level stability is generated in the winter subtropics in the GCM, which plays a considerable role in the heat transport. In contrast, in the scaling theory and idealised simulations, essentially all of the required static stability is generated near the tropopause. The low level stability also allows the surface and low level atmosphere to have strong temperature gradients across the tropics, somewhat in the fashion of the surface temperature in the optically thin case we have considered in the present work. We think the most likely candidate for generation of low-level static stability in the GCM Snowball simulations is thermal transience – the fact that the low levels cool much faster in the course of the seasonal cycle than do the upper layers, which moreover helps to suppress convection. It is also possible that eddy heat fluxes in the winter hemisphere are playing a role. The question will have to be resolved in future work involving seasonally varying idealised simulations and parametrized eddy fluxes.

9. Conclusions

We have presented a semi-analytical theory for the depth, width and strength of the steady-state, axisymmetric, nearly-inviscid Hadley cell in a dry band-semigrey atmosphere. A major limitation of this theory is its disregard of the potentially overwhelming effect of horizontal momentum transport by zonally asymmetric eddies (Walker and Schneider, 2006), which may make the predictions of axisymmetric theories irrelevant to the full 3-dimensional

DOI: 10.1002/qj

general circulation. Though we have shown some success in comparing the present theory to full GCM simulations of planetary atmospheres, it should be realised that this success may be fortuitous (section 8).

A related caveat is that the nearly-inviscid assumption is particularly delicate in the present dry context, where convection is active throughout the troposphere (unlike the moist case in which convection is generally suppressed in the subsiding branch of the cell). Vertical momentum transport by convection can be strong in dry boundary layers on Earth, and could destroy the AM conservation on which the present theory is based. On the other hand, numerical simulations (e.g. Figure 11) show that convection is in fact suppressed in the upper branch of the Hadley cell, which is the key region for AM conservation. In fact, we argued in section 6 that this suppression is not incidental but is essential to the functioning of the cell – if convection were not suppressed, the cell could transport no heat and thus could not convert available potential energy to sustain itself against dissipation. Moreover, convection is not present in the stratosphere, so this caveat does not apply to the deep cell. In any case, assessing the effects of convective momentum transport remains an important goal for future work.

A further limitation, discussed in section 3, is the assumption of a negligible difference between surface and near-surface temperature. The difference can be significant under strong insolation and weak surface exchange coefficient, in which case the predicted tropopause level will be in error. Comparison with GCM results for Mars and Snowball Earth (section 8) suggest that the error is not severe in those two cases, however.

We summarise our main conclusions as follows:

(i) Tropopause height depends on optical depth τ_∞, bandwidth β, the ratio $\kappa = R/c_p$ and the degree of pressure broadening. At large τ_∞ and/or small β, the tropopause is either near the ground ($\kappa > 1/4$) or near the top of the atmosphere ($\kappa < 1/4$). Pressure broadening always raises the tropopause. There is no dependence on insolation; as a result, the tropopause is horizontal.

(ii) The circulation always consists of two cells: a strong, relatively narrow cell entirely contained in the troposphere, embedded in a weaker, broader 'deep' cell which embraces both troposphere and stratosphere.

(iii) Under equatorially symmetric insolation, cell width $\varphi_\mathrm{H} = (5\,A\,Ro/3)^{1/2}$, where A depends only on the radiative-convective parameters mentioned in (i) while Ro depends only on insolation, planetary radius and rotation rate. There is no dependence on the gravitational acceleration or on the total mass of the atmosphere (except indirectly through τ_∞).

(iv) The cell width predicted by this theory is smaller than that of HH, but over a broad parameter range the difference is negligible.

(v) A is always greater for the deep cell than for the tropospheric cell, so the former is always wider than the latter. Heat transport depends only on cell width, so the deep cell always carries more heat than the tropospheric cell.

(vi) The tropospheric cell generates non-zero static stability within the subsiding branch partly by horizontally homogenizing upper-tropospheric temperature to the equatorial value and partly by advecting stratospheric air with relatively high potential temperature into the subtropical subsiding region. This self-generated static stability allows the cell to transport energy.

(vii) The meridional energy transport $F_h \sim a^2 S_0 \Delta_s \varphi_\mathrm{H}^3$. The mass flux V also scales as φ_H^3 except for tropospheric cells broader than 20°. The mass flux and energy transport vanish in the optically-thin limit $\tau_\infty \to 0$, which can be understood as a consequence of Sandström's effect.

(viii) Under solstitial conditions, $\varphi_\mathrm{H} = (cA\,Ro)^{1/3}$, where c is an empirical constant.

(ix) The theory compares very well with axisymmetric numerical simulations. Cell widths compare reasonably well with full GCM simulations of Mars and Snowball Earth under both equinoctial and solstitial conditions, but Hadley cell mass fluxes are overestimated by a large factor, especially in the troposphere.

Acknowledgments

We thank the three anonymous reviewers for insightful and constructive comments. The work was supported by US National Science Foundation grant ATM-0121028.

Appendix

Derivation of band-semigrey radiative equilibrium solutions and tropopause height equation.

We present here details of the derivation of (21)–(23). The derivation is facilitated by defining

$$F_\lambda = I_\lambda^+ - I_\lambda^-, \tag{A.1}$$

$$J_\lambda = I_\lambda^+ + I_\lambda^-, \tag{A.2}$$

so that the radiative transfer equations (8) and (9) take the form

$$\frac{dF_\lambda}{d\tau_\lambda} = -J_\lambda + 2\pi B_\lambda, \tag{A.3}$$

$$\frac{dJ_\lambda}{d\tau_\lambda} = -F_\lambda, \tag{A.4}$$

with boundary conditions

$$F_\lambda = J_\lambda \qquad \text{at the top,} \tag{A.5}$$

$$F_\lambda + J_\lambda = 2B_\lambda(T_s) \qquad \text{at the surface.} \tag{A.6}$$

DOI: 10.1002/qj

Radiative equilibrium and planetary radiative balance imply

$$\int_0^\infty F_\lambda \, \mathrm{d}\lambda = F_\mathrm{b} + (1-\beta)\sigma T_s^4 = S, \tag{A.7}$$

where $F_\mathrm{b} = \int_{\lambda_1}^{\lambda_2} F_\lambda \mathrm{d}\lambda$. Integrating (A.1) over wavelength then gives

$$J_\mathrm{b} = 2\beta\sigma T^4, \tag{A.8}$$

where $J_\mathrm{b} = \int_{\lambda_1}^{\lambda_2} J_\lambda \mathrm{d}\lambda$. Integrating (A.2) over wavelength and vertically up to the top of the atmosphere yields

$$J_{\mathrm{b}\infty} - J_\mathrm{b} = -F_\mathrm{b}(\tau_{\mathrm{b}\infty} - \tau_\mathrm{b}),$$

which, using boundary condition (A.5), leads to

$$J_\mathrm{b} = F_\mathrm{b}(1 + \tau_{\mathrm{b}\infty} - \tau_\mathrm{b}). \tag{A.9}$$

Analogously, integrating (A.2) up from the surface and using boundary condition (A.6) gives

$$J_\mathrm{b} = 2\beta\sigma T_\mathrm{s}^4 - F_\mathrm{b}(1 + \tau_\mathrm{b}). \tag{A.10}$$

(A.7)–(A.10) are four equations in the four unknowns F_b, J_b, T and T_s, which can be trivially solved to yield the radiative equilibrium temperature structure (21), (22).

To derive the equation for tropopause height we proceed as follows. Firstly, note that by definition $I_\mathrm{b}^+ = (F_\mathrm{b} + J_\mathrm{b})/2$. Using (A.8) and (A.9) evaluated just above the tropopause, where radiative equilibrium prevails, we have

$$I_\mathrm{bt}^+ = \left(\frac{2 + \tau_{\mathrm{b}\infty} - \tau_\mathrm{b}}{1 + \tau_{\mathrm{b}\infty} - \tau_\mathrm{b}}\right)\beta\sigma T_\mathrm{t}^4, \tag{A.11}$$

where subscript t indicates quantities evaluated just above the tropopause. On the other hand, we can explicitly evaluate the upwelling radiative flux at the tropopause using (12). Given that the tropospheric temperature profile follows the dry adiabat, so that $T = T_\mathrm{t}(\eta/\eta_\mathrm{t})^\kappa$, and assuming the the difference between surface temperature and near-surface atmospheric temperature is small enough to be neglected, we have

$$I_\mathrm{bt}^+ = \eta_\mathrm{t}^{-4\kappa}\left(\int_0^{\tau_\mathrm{bt}} \eta^{4\kappa}\mathrm{e}^{\tau_\mathrm{b}-\tau_\mathrm{bt}}\,\mathrm{d}\tau_\mathrm{b} + \mathrm{e}^{-\tau_\mathrm{bt}}\right)\beta\sigma T_\mathrm{t}^4, \tag{A.12}$$

where subscript t now indicates quantities evaluated just below the tropopause. Imposing that both T and I_b^+ be continuous across the tropopause allows us to equate (A.11) and (A.12), leading to (23).

References

Barnes JR, Haberle RM. 1996. The Martian zonal-mean circulation: Angular momentum and potential vorticity structure in GCM simulations. *J. Atmos. Sci.* **53**: 3143–3156.

Defant A. 1961. *Physical Oceanography*. Pergamon Press: New York.

Elsasser WM. 1942. *Heat transfer by infrared radiation in the atmosphere*. *Harvard Meteorological Studies*, Vol. 6. Harvard University Press.

Forget F, Pierrehumbert RT. 1997. Warming early Mars with carbon dioxide clouds that scatter infrared radiation. *Science* **278**: 1273–1276.

Forget F, Hourdin F, Fournier R, Hourdin C, Talagrand O, Collins M, Lewis SR, Read PL, Huot J-P. 1999. Improved general circulation models of the Martian atmosphere from the surface to above 80 km. *J. Geophys. Res.* **104**: 24155–24176, 10.1029/1999JE001025.

Goody RM, Yung YL. 1989. *Atmospheric Radiation: Theoretical Basis*. Oxford University Press: Oxford, UK.

Hadley G. 1735. Concerning the cause of the general trade winds. *Phil. Trans. R. Soc. London* **29**: 58–62.

Held IM. 1982. On the height of the tropopause and the static stability of the troposphere. *J. Atmos. Sci.* **32**: 412–417.

Held IM, Hou AY. 1980. Nonlinear axially symmetric circulations in a nearly inviscid atmosphere. *J. Atmos. Sci.* **37**: 515–533.

Hoffman PF, Kaufman AJ, Halverson GP, Schrag DP. 1998. A Neoproterozoic snowball Earth. *Science* **281**: 1342–1346.

Leovy C. 2001. Weather and climate on Mars. *Nature* **412**: 245–249.

Lewis SR. 2003. Modelling the Martian atmosphere. *Astron. Geophys.* **44**: 6–14, 10.1046/j.1468-4004.2003.44406.x.

Lindzen RS, Hou AY. 1988. Hadley circulations for zonally averaged heating centered off the equator. *J. Atmos. Sci.* **45**: 2416–2427.

Lorenz EN. 1967. *The nature and theory of the general circulation of the atmosphere*. Report No. 218, World Meteorological Organization: Geneva, Switzerland.

Mitchell JL, Pierrehumbert RT, Frierson DMW, Caballero R. 2006. The dynamics behind Titan's methane clouds. *Proc. Natl. Acad. Sci. USA* **49**: 18421–18426, doi: 10.1073/pnas.0605074 103.

Paparella F, Young WR. 2002. Horizontal convection is non-turbulent. *J. Fluid Mech.* **466**: 205–214.

Pauluis O. 2004. Boundary layer dynamics and the cross-equatorial Hadley circulation. *J. Atmos. Sci.* **61**: 1161–1173.

Peixoto JP, Oort AH. 1992. *Physics of Climate*. American Institute of Physics: New York.

Pierrehumbert RT. 2005. Climate dynamics of a hard snowball Earth. *J. Geophys. Res.* **110**: D1111, doi: 10.1029/2004JD005 162.

Sandström JW. 1908. Dynamische Versuche mit Meerwasser. *Annalen der Hydrographie under Maritimen Meteorologie* **36**: 6–23.

Schneider EK. 1977. Axially symmetric steady-state models of the basic state for instability and climate studies. Part II: Nonlinear calculations. *J. Atmos. Sci.* **34**: 280–296.

Schneider T. 2004. The tropopause and the thermal stratification in the extratropics of a dry atmosphere. *J. Atmos. Sci.* **61**: 1317–1340.

Thuburn J, Craig GC. 2000. Stratospheric influence on tropopause height: The radiative constraint. *J. Atmos. Sci.* **57**: 17–28.

Vallis GK. 2006. *Atmospheric and Oceanic Fluid Dynamics*. Cambridge University Press: Cambridge, UK.

Walker CC, Schneider T. 2006. Eddy influences on Hadley circulations: Simulations with an idealized GCM. *J. Atmos. Sci.* **63**: 3333–3350.

Weaver CP, Ramanathan V. 1995. Deductions from a simple climate model: Factors governing surface temperature and atmospheric thermal structure. *J. Geophys. Res.* **100**: 11585–11592, 10.1029/95JD00770.